

Decoding Vibrational Signatures of Molybdenum Sulphide Molecular Catalysts for Solar Hydrogen Evolution

Pardis Adams,^a Jan Bühler,^a Angel Labordet Alvarez,^{b,c} S. David Tilley,^a and Mirjana Dimitrievska^{*b}

Received 00th January 20xx,
Accepted 00th January 20xx

DOI: 10.1039/x0xx00000x

Molybdenum sulphide clusters $[\text{Mo}_3\text{S}_4]^{4+}$ and $[\text{Mo}_3\text{S}_{13}]^{2-}$ have emerged as critical molecular models for understanding active sites in Mo–S-based catalysts, as well as promising candidates for energy conversion applications. Despite their relevance, the comprehensive vibrational characterisation of these clusters remains limited. Here, a detailed Raman and infrared spectroscopic analysis of both $[\text{Mo}_3\text{S}_4]^{4+}$ and $[\text{Mo}_3\text{S}_{13}]^{2-}$ is presented, supported by density functional theory (DFT) calculations. High-quality crystalline samples were prepared and characterised using scanning electron microscopy (SEM) and energy-dispersive X-ray spectroscopy (EDX) to confirm morphology and stoichiometry. Raman spectra were acquired using 488 nm and 532 nm laser excitation and deconvoluted using rigorous methodology with Lorentzian curves. The resulting Raman peak frequencies were assigned through direct comparison with DFT-predicted vibrational modes. For $[\text{Mo}_3\text{S}_4]^{4+}$, prominent Raman bands appear around 200 cm^{-1} , 350 cm^{-1} , and 450 cm^{-1} , corresponding to Mo–S–Mo bending, Mo–S stretching, and terminal S-related vibrations, respectively. $[\text{Mo}_3\text{S}_{13}]^{2-}$ exhibits two distinct spectral regions: the $100\text{--}400\text{ cm}^{-1}$ range dominated by Mo–S and S–S bending and stretching, and the $450\text{--}550\text{ cm}^{-1}$ region associated with strong S–S terminal disulphide stretching. Complementary calculations of the IR spectra revealed additional vibrational features, providing a more complete fingerprint for each cluster. Finally, the superior sensitivity of Raman spectroscopy over X-ray diffraction (XRD) for identifying these clusters when supported on other types of materials is demonstrated. This work provides a detailed vibrational reference for $[\text{Mo}_3\text{S}_4]^{4+}$ and $[\text{Mo}_3\text{S}_{13}]^{2-}$, establishing Raman and IR spectroscopy as robust techniques for characterising Mo–S molecular clusters in both fundamental and applied research.

Introduction

Molybdenum sulphide (Mo_xS_y) clusters have emerged as a promising class of catalysts for a wide range of chemical transformations, particularly in sustainable energy and green chemistry.^{1,2} Among these, molecular clusters such as $[\text{Mo}_3\text{S}_4]^{4+}$ and $[\text{Mo}_3\text{S}_{13}]^{2-}$ have attracted increasing interest due to their well-defined structures, tunable reactivity, and capacity to mimic the active sites of heterogeneous molybdenum sulphide catalysts.^{3,4} Molybdenum disulphide (MoS_2), a layered transition metal dichalcogenide, has long been recognised for its catalytic activity in hydrodesulphurisation (HDS)^{5,6} and, more recently, for the hydrogen evolution reaction (HER)^{7–10}. However, its catalytic performance is primarily governed by edge sites, which are difficult to control and characterise in bulk materials.^{11–14} On the other hand, molecular clusters such as $[\text{Mo}_3\text{S}_4]^{4+}$ and $[\text{Mo}_3\text{S}_{13}]^{2-}$ provide a structurally precise and atomically defined alternative with tuneable redox properties. These clusters serve as a model system for understanding active sites in heterogeneous catalysts, allowing systematic

investigation of structure-activity relationships and facilitating mechanistic insights at the molecular level.^{15–17} The $[\text{Mo}_3\text{S}_4]^{4+}$ cluster, often seen as a core motif in larger molybdenum sulphide clusters and MoS_2 edge sites,^{18,19} comprises a Mo_3 triangle with an apical sulphur atom and bridging sulphide ligands (Fig. 1a). This cluster has been explored for its ability to mediate multi-electron transformations and is particularly interesting as a structural analogue to biological molybdenum cofactors found in enzymes such as nitrogenases and sulphite oxidases.^{2,20–23} Similarly, the $[\text{Mo}_3\text{S}_{13}]^{2-}$ cluster features a triangular molybdenum core bridged by sulphur atoms and capped with terminal disulphide ligands (Fig. 1b). This structure exhibits rich redox chemistry and accessible active sites that can catalyse electron and proton transfer cycles.^{24,25} Studies have shown that $[\text{Mo}_3\text{S}_{13}]^{2-}$ can catalyse HER with performance metrics approaching those of bulk MoS_2 while providing a molecular platform amenable to fine-tuning through ligand substitution or cluster derivatisation.^{26–32} Collectively, $[\text{Mo}_3\text{S}_4]^{4+}$ and $[\text{Mo}_3\text{S}_{13}]^{2-}$ represent key models for understanding catalytic processes at Mo–S active sites.^{2,33,34} Their modularity enables a bottom-up approach to catalyst design, bridging the gap between molecular and solid-state catalysis.^{3,24,35} Continued exploration and comprehensive characterisation of these clusters hold promise for advancing the rational development of new catalysts for hydrogen generation, CO_2 reduction, and other sustainable chemical processes.^{36–38} Raman spectroscopy has proven to be an indispensable technique for characterising

^a Department of Chemistry, University of Zurich, Zurich, Switzerland.

^b Transport at Nanoscale Interfaces, EMPA, Dübendorf, Switzerland. E-mail: Mirjana.Dimitrievska@empa.ch

^c Department of Physics and Swiss Nanoscience Institute, University of Basel, Basel, Switzerland

Supplementary Information available: [details of any supplementary information available should be included here]. See DOI: 10.1039/x0xx00000x

these molecular clusters.^{39–47} As a vibrational analysis technique, Raman spectroscopy offers detailed fingerprints for identifying structural motifs and ligand environments. It also functions as an effective probe for assessing compositional integrity and observing transformations under operando conditions.⁴⁸ In particular, for clusters like $[\text{Mo}_3\text{S}_4]^{4+}$ and $[\text{Mo}_3\text{S}_{13}]^{2-}$, where sulphur coordination and bonding are central to the function, Raman spectroscopy can reveal detailed information about metal–sulphur and sulphur–sulphur interactions. To date, Raman data for $[\text{Mo}_3\text{S}_4]^{4+}$ and $[\text{Mo}_3\text{S}_{13}]^{2-}$ have been reported in a few studies, but typically in a partial or application-specific context.⁴⁹ For example, Raman spectra of $[\text{Mo}_3\text{S}_{13}]^{2-}$ have been observed during electrocatalytic operation and thin-film preparation, often showing characteristic bands in the 200–550 cm^{-1} range associated with Mo–S and S–S vibrations.²⁵ Similarly, $[\text{Mo}_3\text{S}_4]^{4+}$ species have been investigated as precursors or intermediates in sulphide synthesis, but their complete vibrational assignments are rarely presented or compared to density functional theory (DFT) calculations.⁵⁰ This lack of a well-established vibrational reference dataset poses challenges for researchers aiming to synthesise, characterise, or detect these clusters reliably, especially in complex or hybrid materials environments. This study addresses this need by providing a complete vibrational characterisation of the $[\text{Mo}_3\text{S}_4]^{4+}$ and $[\text{Mo}_3\text{S}_{13}]^{2-}$ clusters using a combined experimental and computational approach. This begins by preparing high-quality crystalline samples of each cluster and verifying their morphology, composition, and stoichiometry using scanning electron microscopy (SEM) and energy-dispersive X-ray spectroscopy (EDX). Raman spectroscopic measurements are performed using two excitation wavelengths (532 nm and 488 nm), allowing us to probe resonance effects and improve mode detection across a broad spectral range. These measurements are directly compared with DFT predictions, enabling the assignment of all experimentally observed Raman modes. In parallel, the calculated infrared (IR) vibrational spectra are reported, and the corresponding IR-active modes are identified for both clusters. By presenting both Raman and IR signatures along with full DFT-supported assignments, a comprehensive vibrational fingerprint for $[\text{Mo}_3\text{S}_4]^{4+}$ and $[\text{Mo}_3\text{S}_{13}]^{2-}$ is established. This approach supports the precise identification of these clusters and opens new avenues for extending their characterisation via IR spectroscopy, particularly in environments where Raman scattering may be limited.

Results and discussion

Structural Overview of $[\text{Mo}_3\text{S}_4]^{4+}$ and $[\text{Mo}_3\text{S}_{13}]^{2-}$ Clusters

The molecular structures of $[\text{Mo}_3\text{S}_4]^{4+}$ and $[\text{Mo}_3\text{S}_{13}]^{2-}$ are shown in Fig. 1, highlighting the differences in nuclearity, sulphur coordination, and symmetry that underlie their spectroscopic behaviour and chemical functionality. The $[\text{Mo}_3\text{S}_4]^{4+}$ cluster in Fig. 1a features a triangular arrangement of three Mo atoms bridged by a tetrahedral sulphur ligand environment.

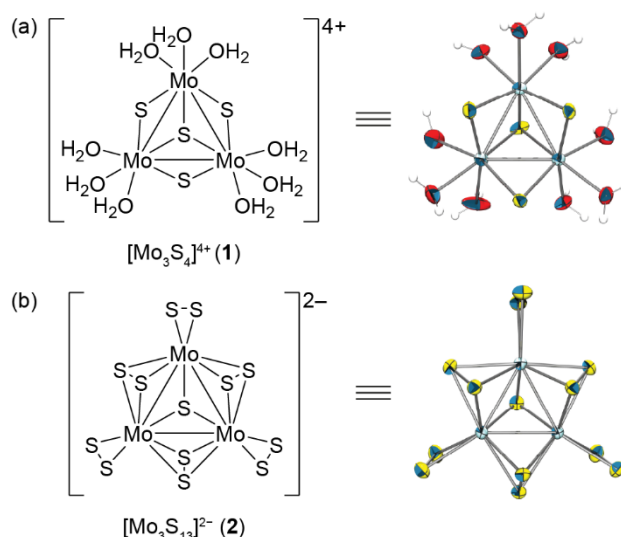


Fig. 1 Molecular structure and ellipsoid displacement plots of (a) $[\text{Mo}_3\text{S}_4]^{4+}$ and (b) $[\text{Mo}_3\text{S}_{13}]^{2-}$. Ellipsoids represent 50% probability. Solvent molecules and counterions (Cl^- for (b) and NH_4^+ for (c)) are omitted for clarity. Figure modified from⁴⁹.

The cluster includes three μ_2 -sulphide ligands, sulphide ions (S^{2-}) that bridge two Mo atoms along the triangle's edges, and a single μ_3 -sulphide that caps one face of the triangle by coordinating all three Mo atoms. Crystallographic data^{49,51,52} show that the Mo–Mo distances range from 2.801 to 2.82 Å, indicating significant metal–metal bonding. The Mo–S bond lengths vary depending on the coordination environment: Mo–(μ_2 -S) bonds are typically 2.28–2.30 Å, while Mo–(μ_3 -S) bonds are slightly longer, ranging from 2.32–2.33 Å, due to the higher coordination number of the apical sulphur atom. Each Mo centre adopts a distorted tetrahedral geometry, coordinated by two bridging sulphides, one apical μ_3 -sulphide, and one or more metal–metal interactions. This compact, symmetric configuration reflects structural motifs found at catalytically active edge sites in MoS_2 and provides a molecular model for sulphur-mediated multi-electron processes.^{3,53} In contrast, the $[\text{Mo}_3\text{S}_{13}]^{2-}$ cluster, shown in Fig. 1b, exhibits a more open and sulphur-rich architecture. It contains a similar triangular Mo_3 core but is surrounded by thirteen sulphur atoms, comprising both terminal and bridging species. Notably, the cluster includes six terminal disulphide (S_2^{2-}) ligands, each coordinating to a Mo centre. These disulphides show Mo–S bond lengths in the range of 2.38–2.45 Å, which are longer than those of bridging sulphides, reflecting weaker Mo–S interactions. The remaining sulphur atoms form a combination of μ_2 - and μ_3 -bridging ligands, with Mo–S distances typically between 2.30–2.36 Å for μ_2 -S and up to 2.40 Å for μ_3 -S bridges.

Morphological and Compositional Analysis

To verify the crystallinity, morphology, and elemental composition of the prepared clusters, scanning electron microscopy (SEM) and energy-dispersive X-ray spectroscopy (EDX) was performed on isolated crystals of $[\text{Mo}_3\text{S}_4]^{4+}$ and $[\text{Mo}_3\text{S}_{13}]^{2-}$. These analyses are crucial to confirm that the synthetic procedures yield phase-pure, structurally intact

materials prior to spectroscopic characterisation. Fig. 2 shows SEM images and corresponding compositional maps of Sn, S and Mo measured with EDX. The presence of tin (Sn) in the spectra is attributed to the use of fluorine-doped SnO₂-coated (FTO) substrates during the measurements. SEM imaging revealed well-defined microcrystals with distinct morphological features reflective of their underlying structural and packing motifs. As observed in Fig. 2a, crystals of [Mo₃S₄]⁴⁺ appear as uniform, prismatic blocks, consistent with compact molecular packing driven by the cluster's relatively symmetric, triangular core structure. In contrast, Fig. 2e shows that [Mo₃S₁₃]²⁻ forms more irregular, platelet-like crystallites, which may be attributed to its higher sulphur content, extended ligand shell, and more open coordination environment. These morphological differences align with the divergent molecular architectures of the two clusters and suggest that subtle variations in cluster geometry influence their nucleation and growth behaviour during crystallisation. EDX analysis in Fig. 2b-d and Fig. 2f-h confirmed the elemental composition of both clusters, with clearly resolved molybdenum and sulphur signals. As determined by EDX, shown in Table S1, the Mo:S atomic ratio for [Mo₃S₄]⁴⁺ was approximately 0.83±0.10, in good agreement with the theoretical value of 0.75. For [Mo₃S₁₃]²⁻, the Mo:S ratio was found to be 0.31±0.10, compared to the ideal 0.23 expected from the cluster stoichiometry. Both values are in agreement with the theoretically expected stoichiometry within the error limit. The underrepresentation of sulphur may be attributed to the limited sensitivity of EDX to light elements, particularly when present in the terminal disulphide (S₂²⁻) form. Additionally, the close energy spacing between the Mo M α and S K α emission lines (~2.29 and ~2.31 keV, respectively) can lead to peak overlap, introducing further uncertainty in independent quantification. Altogether, the single crystal XRD, SEM and EDX results confirm both clusters' morphology and elemental composition and provide a solid basis for the following vibrational spectroscopic analysis.

Raman Spectroscopy and Vibrational Mode Assignment

Before analysing the vibrational spectra of [Mo₃S₄]⁴⁺ and [Mo₃S₁₃]²⁻, it is essential to consider the symmetry of the molecular structures, as symmetry dictates the selection rules

and classification of normal modes into irreducible representations. In an idealised, isolated form, the [Mo₃S₄]⁴⁺ cluster possesses a nearly equilateral triangular Mo₃ core capped by a μ_3 -sulphide and bridged by three μ_2 -sulphides. This geometry approximates C_{3v} point group symmetry, resulting in a set of Raman-active A₁ and E modes and IR-active E modes.⁵⁴⁻⁵⁶ [Mo₃S₁₃]²⁻ cluster is more complex due to the presence of multiple inequivalent disulphide ligands and asymmetric bridging sulphurs. In this case, the overall structure lacks symmetry elements beyond identity and is best described by the C₁ point group. In this case, all vibrational modes are formally active in both Raman and infrared spectroscopy, and no degeneracy or selection rules apply. Furthermore, even in the case of [Mo₃S₄]⁴⁺, deviations from idealised symmetry due to crystal packing effects, solvation, or thermal distortions can reduce the effective symmetry below C_{3v}. To treat both clusters consistently and to enable detailed comparison between experiment and theory, vibrational mode analysis and DFT calculations were performed assuming no symmetry constraints (C₁). This approach ensures that all vibrational degrees of freedom are included, and that subtle distortions and mode couplings are captured in the calculations and, therefore, in the calculated vibrational mode properties. Following the symmetry considerations, Fig. 3 presents the experimental and DFT-calculated Raman spectra of the [Mo₃S₄]⁴⁺ and [Mo₃S₁₃]²⁻ clusters. The upper panels show the measured spectra obtained using 532 nm and 488 nm excitation wavelengths, highlighting all Raman-active vibrational modes observed under ambient conditions. Both excitation sources yielded consistent results, with no significant resonance enhancement or wavelength-dependent shifts, confirming the robustness of the spectral features across these two excitation energies. The corresponding DFT-calculated Raman spectra are displayed in black alongside the experimental ones in Fig. 3e. These theoretical Raman spectra were obtained from DFT calculations performed without symmetry constraints (C₁ point group) to fully account for all Raman-active normal modes, including those arising from subtle structural distortions. The calculated spectra were normalised to align with the experimental data and allow direct mode-by-mode comparison.

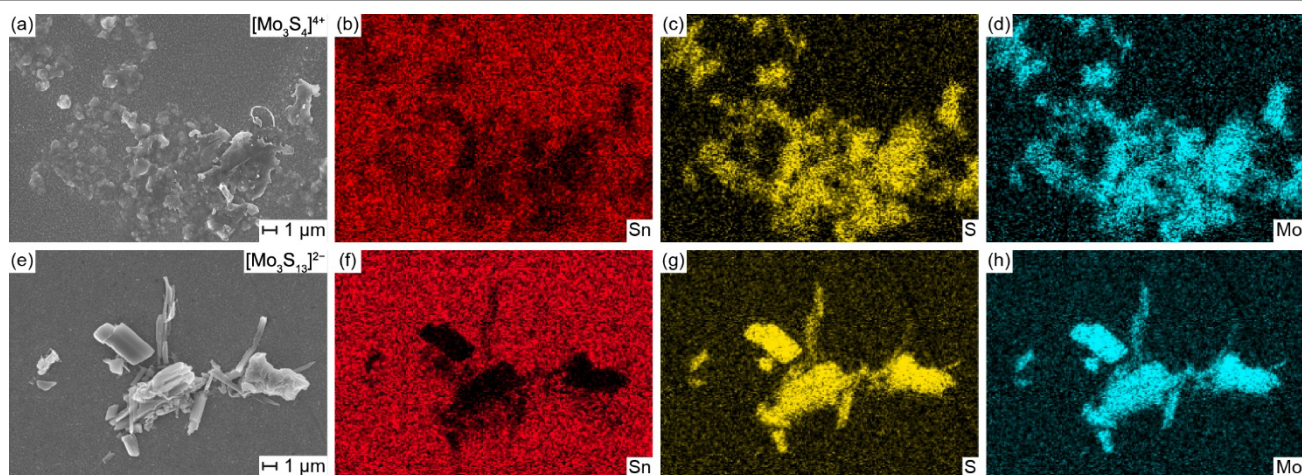


Fig. 2 SEM spectra and EDX mapping of Sn, S and Mo for (a-d) [Mo₃S₄]⁴⁺, (e-h) [Mo₃S₁₃]²⁻.

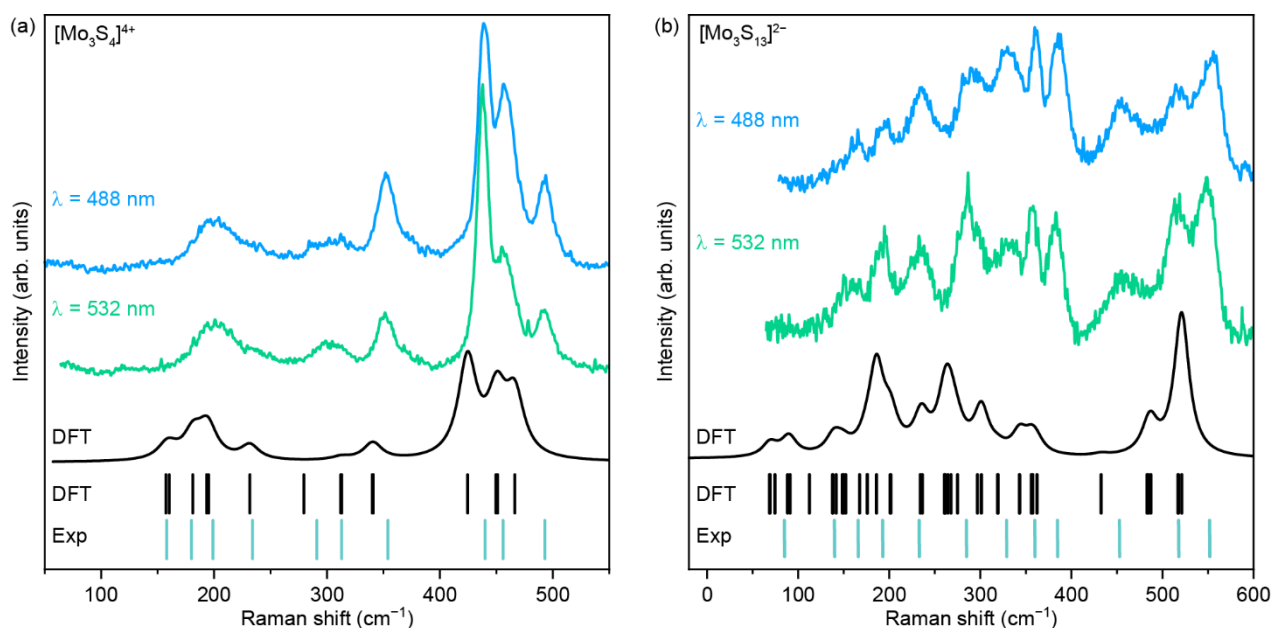


Fig. 3 Raman spectra of (a) $[\text{Mo}_3\text{S}_4]^{4+}$ and (b) $[\text{Mo}_3\text{S}_{13}]^{2-}$ measured using 488 nm and 532 nm laser excitation and compared with DFT-calculated Raman spectra. Vertical lines under the spectrum show a comparison between the Raman peak positions obtained experimentally by the deconvolution (labelled "Exp") and from the lattice dynamics calculations based on DFT (labelled "DFT").

Beneath the spectra, Fig. 3 also displays vertical bars marking the positions of DFT-predicted Raman-active modes and experimentally extracted peak frequencies. Experimental peak frequencies were determined by a rigorous Lorentzian deconvolution procedure, as described in detail by Dimitrievska et al. (2023,2024),^{57,58} allowing accurate separation of overlapping features and assignment of vibrational modes with improved accuracy. This method enabled the identification of weak and partially overlapping peaks that would otherwise be obscured in the spectra, particularly in the congested mid and high-frequency regions of the $[\text{Mo}_3\text{S}_{13}]^{2-}$ spectrum. The experimental and computational analysis results are summarised in Table 1 for $[\text{Mo}_3\text{S}_4]^{4+}$ and Table 2 for $[\text{Mo}_3\text{S}_{13}]^{2-}$, which provide a direct comparison between the experimentally observed Raman frequencies, the corresponding DFT-calculated frequencies, and previously reported values from the literature.^{39–46} These tables also include vibrational assignments for each mode, providing a comprehensive reference dataset for the $[\text{Mo}_3\text{S}_4]^{4+}$ and $[\text{Mo}_3\text{S}_{13}]^{2-}$ cluster families. While the overall agreement between the experimental and DFT-predicted Raman spectra is strong, some discrepancies in peak positions and relative intensities are observed. These are expected and can be attributed to several factors. Frequency deviations between experiment and calculated are usually within $\pm 10 \text{ cm}^{-1}$ or less. Such differences arise from the harmonic approximation used in DFT calculations, neglecting real systems' anharmonic effects.⁵⁹ Additionally, environmental influences such as crystal packing, intermolecular interactions, or solvent residues in the experimental samples can shift vibrational frequencies relative to the isolated-molecule model used in calculations.^{60,61} Differences in Raman intensity between the experimentally obtained and calculated spectra are also more pronounced and commonly observed in

molecular vibrational studies.⁶² While DFT estimates Raman activity based on changes in polarisability, the experimental intensity depends on several additional factors: excitation wavelength, resonance enhancement, local dielectric environment, and instrumental response.⁶³ Moreover, subtle changes in the geometry or symmetry of a cluster, especially in the $[\text{Mo}_3\text{S}_{13}]^{2-}$ case, can lead to significant intensity redistribution among closely spaced modes. In this context, the presence of overlapping bands and the relative weakness of specific low- or high-frequency vibrations may lead to the underrepresentation or absence of certain theoretically predicted peaks in the experimental spectra. Despite these limitations, a very good agreement between the experimentally obtained and DFT-calculated Raman spectra is observed in Fig. 3, providing a solid reference Raman framework for future studies.

Vibrational Nature of Raman Modes in $[\text{Mo}_3\text{S}_4]^{4+}$

In order to better understand the structural dynamics of the $[\text{Mo}_3\text{S}_4]^{4+}$ and $[\text{Mo}_3\text{S}_{13}]^{2-}$ clusters, their vibrational patterns were investigated, and the atomic displacements associated with key Raman-active modes were analysed. This enables the linking of the specific spectral features to distinct types of motion within the Mo–S framework. The vibrational modes of the $[\text{Mo}_3\text{S}_4]^{4+}$ cluster, presented in Fig. S1, reveal a particular interplay between metal–metal and metal–ligand dynamics that reflect the unique structure of the cluster. These figures show the atomic displacement patterns of all vibrational modes of $[\text{Mo}_3\text{S}_4]^{4+}$. Low-frequency modes (e.g., $\sim 157\text{--}195 \text{ cm}^{-1}$) are predominantly characterised by concerted motions of Mo atoms within the Mo_3 triangle.

Table 1. Frequencies (in cm^{-1}) of Raman peaks for $[\text{Mo}_3\text{S}_4]^{4+}$ obtained from Lorentzian fitting of experimental spectra and proposed vibrational mode assignments, compared with DFT-calculated values and literature references.

Experimental (cm^{-1})	DFT (cm^{-1})	Assignment	Literature (cm^{-1})	Reference
158	157, 160	In-plane bending, Mo–S–Mo bridge bend	141–160	Sukhanova et al. (2023) ³⁹
180	181	Mo–S stretch	180–210	Sukhanova et al. (2023) ³⁹
199	193, 195	Mo–Mo + S–bridge coupled mode	~200	Sukhanova et al. (2023) ³⁹
234	231	Symmetric Mo–S–Mo stretch	230–240	Ohki et al. (2019) ⁴⁰
291	280	Asymmetric Mo–S stretch	284	Sukhanova et al. (2023) ³⁹
313	312, 313	Mixed bending/stretching	~310	Tran et al. (2016), ⁴¹ Deng et al. (2016) ⁴²
354	340, 341	Asymmetric S stretch	~350	Ohki et al. (2019) ⁴⁰
440	424	S-atom vibration (terminal/apical)	440	Tran et al. (2016), ⁴¹ Deng et al. (2016) ⁴²
456	449, 451	S–S or Mo–S asymmetric bending	450–460	Tran et al. (2016) ⁴¹
493	466	Terminal S stretch or Mo–S–S	493	Sukhanova et al. (2023) ³⁹

Table 2. Frequencies (in cm^{-1}) of Raman peaks for $[\text{Mo}_3\text{S}_{13}]^{2-}$ obtained from Lorentzian fitting of experimental spectra and proposed vibrational mode assignments, compared with DFT-calculated values and literature references.

Experimental (cm^{-1})	DFT (cm^{-1})	Assignment	Literature (cm^{-1})	Reference
85	88	Mo–S cage deformation	85–90	Xi et al. (2022), ⁴³ Fedin et al. (1989) ⁴⁴
140	137, 138, 142	Internal Mo–S deformation	~140	Tran et al. (2016), ⁴¹ Fedin et al. (1989) ⁴⁴
166	167	In-plane Mo–S bend	160–170	Sukhanova et al. (2023) ³⁹
193	186	Mo–Mo stretch	193	Xi et al. (2022), ⁴³ Müller et al. (1991) ⁴⁵
233	234, 236	Mo–S–Mo bridge motion	~230	Ohki et al. (2019) ⁴⁰
285	275, 297	Asymmetric Mo–S vibration	284–290	Tran et al. (2016) ⁴¹
329	319, 320	Mixed stretching/bending	325–330	Tran et al. (2016) ⁴¹
360	356, 358	S–S bridge bend	~360	Xi et al. (2022) ⁴³
385	362	Terminal S wagging	384	Xi et al. (2022) ⁴³
453	432	S–S symmetric stretch	450–460	Tran et al. (2016), ⁴¹ Müller et al. (1991) ⁴⁵
518	517, 518	Terminal S–S bond vibration	518	Xi et al. (2022), ⁴³ Fedin et al. (1989), ⁴⁴ Weber et al. (1995) ⁴⁶

These motions range from symmetric breathing-like displacements (e.g., 157 cm^{-1}), where all three Mo atoms move in and out synchronously relative to the triangle centre, to shearing or rocking-type modes (e.g., 195 cm^{-1}) involving relative lateral displacements of Mo atoms, which distort the triangle without changing its area. Such metal-core-dominated vibrations are generally indicative of strong Mo–Mo bonding interactions, which are central to the cluster's structural integrity and electronic properties. At intermediate frequencies ($\sim 230\text{--}340 \text{ cm}^{-1}$), the vibrations begin to involve more complex Mo–S stretching and bending, particularly with contributions from the apical sulphur atoms that cap the Mo_3 base. These modes typically display mixed character, where both Mo–Mo

and Mo–S displacements are non-negligible. For instance, the mode near 231 cm^{-1} shows cooperative displacement of all three Mo atoms accompanied by out-of-phase S atom motion, resembling umbrella-like deformations of the Mo_3S_3 unit. In contrast, the higher modes in this region feature localised stretching of Mo–S bonds with minor Mo participation. At higher frequencies ($\sim 424\text{--}466 \text{ cm}^{-1}$), the Raman-active modes are dominated by strong symmetric and asymmetric Mo–S stretching vibrations. These modes typically involve terminal sulphurs bonded to a single Mo centre and represent relatively localised vibrations compared to the lower-frequency delocalised modes. Notably, the 466 cm^{-1} mode exhibits a pronounced symmetric Mo–S stretch consistent with literature

reports of terminal Mo–S bond vibrations in related molybdenum–sulphur systems. Comparison with literature, particularly the works by Sukhanova et al. (2023)³⁹ and Ohki et al. (2019)⁴⁰ confirms the overall trends observed in our calculations. The dominant low-frequency modes reported experimentally (e.g., near 180–200 cm⁻¹) have been attributed to Mo₃ breathing or twisting motions, which aligns well with our assignments. Similarly, the high-frequency features in the ~450–470 cm⁻¹ range are assigned in the literature to terminal Mo–S stretches, consistent with our calculated eigenvectors. Though less discussed experimentally due to their lower Raman intensity, the modes in the intermediate range (300–350 cm⁻¹) are predicted to involve both bending and stretching with partial Mo character, corroborated by the literature.^{42,46} Together, the calculated modes for [Mo₃S₄]⁴⁺ support a coherent vibrational profile that reflects both the core rigidity of the Mo₃ triangle and the flexibility of the surrounding sulphur environment.

Vibrational Mode Description of [Mo₃S₁₃]²⁻

The vibrational spectrum of the [Mo₃S₁₃]²⁻ cluster spans a broad range from below 100 cm⁻¹ up to ~520 cm⁻¹, reflecting the presence of both heavy Mo–Mo/Mo–S framework motions and lighter terminal S–S vibrations. Fig. S2 in the Supporting Information shows the atomic displacement patterns of all vibrational modes of [Mo₃S₁₃]²⁻. The vibrational modes can be categorised into distinct groups based on frequency ranges and atomic character. At the low end of the spectrum (below ~150 cm⁻¹), the modes are dominated by collective torsional and wagging motions involving the rigid Mo₃ triangle and its bridging S ligands (e.g., 68, 74 cm⁻¹). These modes often involve symmetric and antisymmetric twisting of the Mo₃ core, as well as out-of-plane librations of the bridging S atoms that connect Mo centres. Some of these low-frequency modes also include the concerted motion of the terminal disulphide (S₂) units, which oscillate relative to the Mo₃ frame with minimal internal deformation (e.g., 88 cm⁻¹).

More complex Mo–S skeletal deformations are observed in the intermediate range between 150 and 300 cm⁻¹. These include in-plane scissoring and rocking of Mo–S–S units (e.g., 213, 275 cm⁻¹), as well as asymmetric flexing modes of the S₂ bridges. Several modes in this region exhibit a characteristic mixture of metal–ligand motion and internal S–S stretch or bend components, reflecting the hybridised nature of bonding within the cluster. Notably, Mo–S bond stretch and bend vibrations become more prominent here (e.g., 296 cm⁻¹), with some differentiation between inner and outer Mo–S bonds depending on the local geometry. Above 300 cm⁻¹, the vibrations increasingly localise on the sulphur atoms, especially on the terminal S₂ ligands. This includes internal S–S stretching vibrations, where each disulphide unit oscillates nearly independently (e.g., 343, 357 cm⁻¹). These modes exhibit significant Raman activity due to the substantial polarisability changes associated with S–S bond deformation. Near the upper end of the spectrum (above ~480 cm⁻¹), the most localised and high-energy S–S stretching modes are found (e.g., 484, 487 cm⁻¹).

These involve almost pure terminal S–S stretches with minimal coupling to the Mo framework and often appear as sharp peaks in experimental Raman spectra.

Across the vibrational spectrum, symmetry trends can be observed: low-frequency modes tend to preserve the overall molecular symmetry, while high-frequency modes increasingly break symmetry due to the localised nature of the atomic displacements, particularly within terminal ligands. In many cases, the threefold symmetry of the cluster leads to near-degenerate mode pairs or subtle splittings due to structural asymmetry in the relaxed geometry. The rich coupling between Mo–S and S–S motions, particularly in the mid-frequency region, contributes to the vibrational complexity and underscores the mixed covalent/ionic character of bonding in [Mo₃S₁₃]²⁻. These insights are valuable for interpreting experimental Raman and IR spectra, particularly in identifying fingerprint regions associated with S₂ ligands and Mo–S connectivity.

Several of the vibrational features identified here are consistent with previous Raman studies on [Mo₃S₁₃]²⁻ and related clusters. High-frequency bands around 450–520 cm⁻¹, attributed to terminal S–S stretching, were also reported by Xi et al. (2019)⁴³ for [Mo₃S₁₃]²⁻ films on FTO and by Tran et al. (2016)⁴¹ in electrodeposited MoS_x films derived from [Mo₃S₁₃]²⁻. Modes in the 200–300 cm⁻¹ range, linked to Mo–S bending and scissoring, have also been observed in [Mo₃S₁₃]²⁻ based systems, as reported by Ohki et al. (2019).⁴⁰ The analysis expands on these observations, providing a detailed assignment of individual vibrational patterns.

Infrared Spectra and Complementary Vibrational Analysis

In addition to Raman spectroscopy, the infrared (IR) spectra of the [Mo₃S₄]⁴⁺ and [Mo₃S₁₃]²⁻ clusters were also calculated to explore their vibrational fingerprints further and investigate the complementary activity of vibrational modes. The simulated IR spectra, shown in Fig. 4, were derived from DFT calculations performed without symmetry constraints, ensuring that all IR-active modes are represented regardless of symmetry selection rules.

As shown in Fig. 4a, for [Mo₃S₄]⁴⁺, the IR spectrum is dominated by bands in the mid-frequency region between 250 and 500 cm⁻¹, corresponding primarily to Mo–S stretching and Mo–S–Mo bending vibrations. These features largely complement the Raman-active modes. The absence of a high density of IR-active modes in the low-frequency region suggests that these motions, primarily involving Mo–Mo deformation, are only weakly coupled to changes in dipole moment, as expected for metal–metal breathing modes. In contrast, in Fig. 4b, the [Mo₃S₁₃]²⁻ cluster displays a significantly richer IR spectrum, with multiple intense bands extending from 150 to over 500 cm⁻¹. These include strong IR-active vibrations associated with bridging and terminal S–S stretching, particularly in the 450–520 cm⁻¹ region. These modes are prominent in IR due to their strong dipole moment variation, making them particularly useful for confirming the presence and integrity of disulphide ligands. Additionally, the mid-frequency IR-active modes around

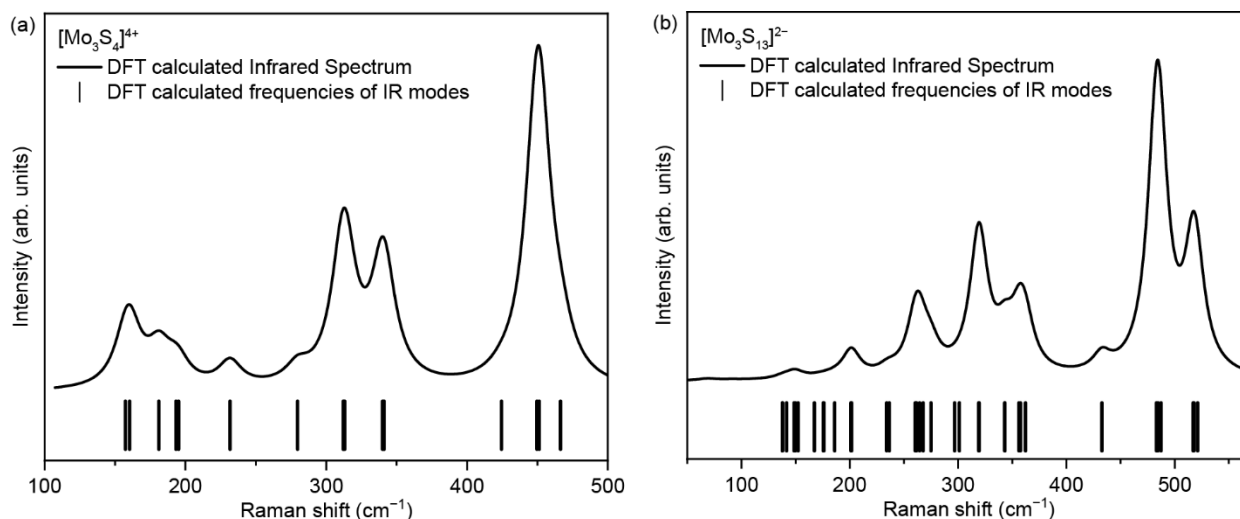


Fig. 4 Calculated infrared (IR) spectra of the $[\text{Mo}_3\text{S}_4]^{4+}$ and $[\text{Mo}_3\text{S}_{13}]^{2-}$ clusters. (a) $[\text{Mo}_3\text{S}_4]^{4+}$ exhibits IR-active modes primarily in the 250–500 cm^{-1} range, corresponding to Mo–S stretching and bending vibrations. (b) $[\text{Mo}_3\text{S}_{13}]^{2-}$ shows a broader and more complex IR spectrum, with intense features in the 150–520 cm^{-1} region, including strong terminal S–S stretching bands above 450 cm^{-1} .

250–350 cm^{-1} provide complementary information on Mo–S–S bending and scissoring vibrations. These calculations highlight the value of IR analysis as a complementary tool for full vibrational mode identification in complex Mo–S clusters. This provides a reference for future experimental IR studies to refine cluster characterisation.

Raman Spectroscopy as a Structural Fingerprinting Tool

Fig. 5 highlights the practical advantage of Raman spectroscopy over X-ray diffraction (XRD) in distinguishing Mo-based clusters deposited on complex substrates. In this example, $[\text{Mo}_3\text{S}_4]^{4+}$ and $[\text{Mo}_3\text{S}_{13}]^{2-}$ clusters were deposited on thin films of Sb_2Se_3 , a

widely studied light-absorbing material for water-splitting photocathodes.^{64–67} The goal was to verify whether the two cluster types could be unambiguously detected when supported on the same photoabsorber substrate. Fig. 5a presents Raman spectra from three samples: bare Sb_2Se_3 , Sb_2Se_3 coated with $[\text{Mo}_3\text{S}_4]^{4+}$, and Sb_2Se_3 coated with $[\text{Mo}_3\text{S}_{13}]^{2-}$. The spectrum of the bare Sb_2Se_3 film shows a typical Raman signature of Sb_2Se_3 , characterised by features in the low- to mid-frequency region (< 250 cm^{-1}). Additional peaks emerge upon deposition of the $[\text{Mo}_3\text{S}_4]^{4+}$ cluster, including characteristic bands above 300 cm^{-1} , consistent with Mo–S stretching identified earlier.

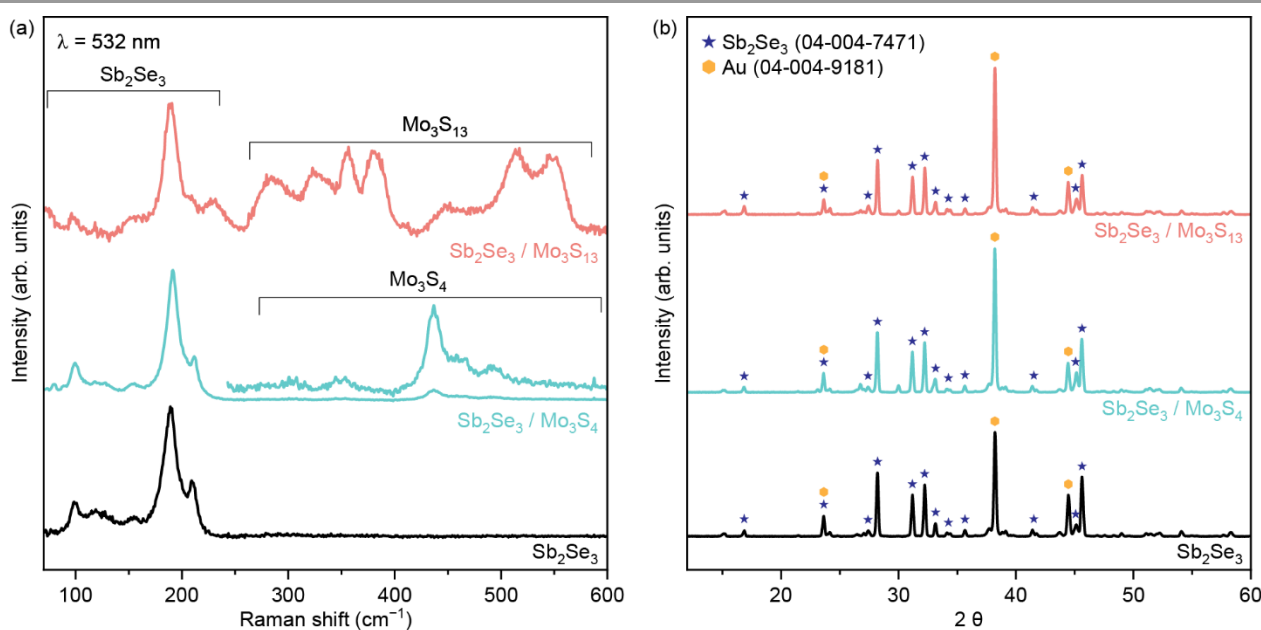


Fig. 5 (a) Raman spectra of Sb_2Se_3 thin films before and after deposition of $[\text{Mo}_3\text{S}_4]^{4+}$ and $[\text{Mo}_3\text{S}_{13}]^{2-}$ clusters. The reference Sb_2Se_3 film shows its characteristic Raman features, while the addition of $[\text{Mo}_3\text{S}_4]^{4+}$ and $[\text{Mo}_3\text{S}_{13}]^{2-}$ introduces distinct vibrational bands corresponding to Mo–S stretching $[\text{Mo}_3\text{S}_4]^{4+}$ and S–S disulphide stretching $[\text{Mo}_3\text{S}_{13}]^{2-}$, enabling precise identification of each cluster. (b) X-ray diffraction (XRD) patterns of the same three samples. No structural changes are observed upon cluster deposition, illustrating the limited sensitivity of XRD compared to Raman spectroscopy for detecting surface-bound molecular species.

In the case of $[\text{Mo}_3\text{S}_{13}]^{2-}$ deposition, several new peaks appear in the high-frequency region, most in the 250–520 cm^{-1} range, corresponding to vibrational pattern of $[\text{Mo}_3\text{S}_{13}]^{2-}$ presented earlier. These features clearly differentiate between the two cluster types and demonstrate Raman's ability to resolve their unique vibrational fingerprints, even when deposited as thin surface layers. In contrast, Fig. 5b presents the corresponding XRD patterns for the same three samples. All patterns exhibit reflections characteristic of the crystalline Sb_2Se_3 phase, but no additional peaks or shifts are observed upon deposition of either cluster. This is likely due to the small size, low crystallinity, or surface-dispersed nature of the Mo clusters, which are often invisible to conventional diffraction techniques. This comparison showcases the superior sensitivity of Raman spectroscopy to short-range structural order and local bonding environments over XRD. In contexts where the clusters are amorphous, disordered, or supported in sub-monolayer quantities, Raman measurements provide clear vibrational signatures that allow unambiguous identification. This highlights its value for fundamental characterisation and in-situ or operando studies of functional catalysts and photoelectrodes.

Conclusions

In this work, a comprehensive vibrational study of the $[\text{Mo}_3\text{S}_4]^{4+}$ and $[\text{Mo}_3\text{S}_{13}]^{2-}$ clusters were carried out through a combination of experimental Raman spectroscopy and first-principles calculations. Raman spectra acquired with 488 nm and 532 nm excitation were compared to DFT-calculated vibrational modes, enabling full mode assignment across the entire frequency range. For $[\text{Mo}_3\text{S}_4]^{4+}$, characteristic Raman bands were observed in the 160–230 cm^{-1} region, associated with Mo_3 core breathing and Mo–S–Mo bending modes, as well as in the 300–460 cm^{-1} range, dominated by Mo–S stretching vibrations. For $[\text{Mo}_3\text{S}_{13}]^{2-}$, a broader vibrational signature was identified, with distinct Raman bands appearing from 70 cm^{-1} up to 520 cm^{-1} , including strong S–S stretching modes around 453 and 518 cm^{-1} —serving as reliable fingerprints for the disulphide ligands. Complementary calculations of the IR spectra provided additional information about the vibrational properties and mode of activity of these clusters. The combined experimental and theoretical analysis presented here establishes a complete vibrational reference for $[\text{Mo}_3\text{S}_4]^{4+}$ and $[\text{Mo}_3\text{S}_{13}]^{2-}$, offering valuable tools for their structural identification. Moreover, it is demonstrated that Raman spectroscopy enables unambiguous detection of these clusters even in complex environments, such as when supported on Sb_2Se_3 photocathodes, where XRD analysis shows no clear indication of their presence. This work establishes a robust framework for spectroscopic identification and structural analysis of Mo_3 -based clusters and serves as a foundation for future studies in catalysis and energy conversion applications.

Author contributions

M.D. and P.A. conceptualised the project, curated and analysed data, and wrote the manuscript. J.B. synthesised the catalyst and aided in the manuscript's visualisation aspects, reviewing and editing. A.L.A. did DFT. M.D. acquired the Raman Data. M.D. and S.D.T. supervised the project.

Conflicts of interest

There are no conflicts to declare.

Data availability

A data availability statement (DAS) is required to be submitted alongside all articles. Please read our [full guidance on data availability statements](#) for more details and examples of suitable statements you can use.

Acknowledgements

P.A. acknowledges financial support from the UZH Entrepreneur Fellowship of the University of Zürich, reference no. [SUSEF24-001]. P.A. and S.D.T. would like to thank the University of Zürich and the Swiss National Science Foundation (Project #214810) for support.

References

- 1 L. R. L. Ting, Y. Deng, L. Ma, Y. J. Zhang, A. A. Peterson and B. S. Yeo, *ACS Catal*, 2016, **6**, 861–867.
- 2 S. Batool, M. Langer, S. N. Myakala, M. Heiland, D. Eder, C. Streb and A. Cherevan, *Advanced Materials*, 2024, **36**, 2305730.
- 3 M. L. Grutza, A. Rajagopal, C. Streb and P. Kurz, *Sustain Energy Fuels*, 2018, **2**, 1893–1904.
- 4 J. Kibsgaard, T. F. Jaramillo and F. Besenbacher, *Nature Chemistry* 2014 6:3, 2014, **6**, 248–253.
- 5 R. V. Mom, J. N. Louwen, J. W. M. Frenken and I. M. N. Groot, *Nature Communications* 2019 10:1, 2019, **10**, 1–8.
- 6 M. K. Prabhu, J. N. Louwen, E. T. C. Vogt and I. M. N. Groot, *Nature Communications* 2024 15:1, 2024, **15**, 1–17.
- 7 G. Ye, Y. Gong, J. Lin, B. Li, Y. He, S. T. Pantelides, W. Zhou, R. Vajtai and P. M. Ajayan, *Nano Lett*, 2016, **16**, 1097–1103.
- 8 J. D. Benck, T. R. Hellstern, J. Kibsgaard, P. Chakhranont and T. F. Jaramillo, *ACS Catal*, 2014, **4**, 3957–3971.
- 9 J. Mao, Y. Wang, Z. Zheng and D. Deng, *Front Phys (Beijing)*, 2018, **13**, 1–19.
- 10 A. B. Laursen, S. Kegnaes, S. Dahl and I. Chorkendorff, *Energy Environ Sci*, 2012, **5**, 5577–5591.
- 11 G. Li, D. Zhang, Q. Qiao, Y. Yu, D. Peterson, A. Zafar, R. Kumar, S. Curtarolo, F. Hunte, S. Shannon, Y. Zhu, W. Yang and L. Cao, *J Am Chem Soc*, 2016, **138**, 16632–16638.
- 12 Y. Xu, R. Ge, J. Yang, J. Li, S. Li, Y. Li, J. Zhang, J. Feng, B. Liu and W. Li, *Journal of Energy Chemistry*, 2022, **74**, 45–71.

- 13 J. Zhu, Z. C. Wang, H. Dai, Q. Wang, R. Yang, H. Yu, M. Liao, J. Zhang, W. Chen, Z. Wei, N. Li, L. Du, D. Shi, W. Wang, L. Zhang, Y. Jiang and G. Zhang, *Nature Communications* 2019 10:1, 2019, **10**, 1–7.
- 14 L. Wu, A. Longo, N. Y. Dzade, A. Sharma, M. M. R. M. Hendrix, A. A. Bol, N. H. de Leeuw, E. J. M. Hensen and J. P. Hofmann, *ChemSusChem*, 2019, **12**, 4383–4389.
- 15 B. Lassalle-Kaiser, D. Merki, H. Vrubel, S. Gul, V. K. Yachandra, X. Hu and J. Yano, *J Am Chem Soc*, 2015, **137**, 314–321.
- 16 P. D. Tran, T. V. Tran, M. Orio, S. Torelli, Q. D. Truong, K. Nayuki, Y. Sasaki, S. Y. Chiam, R. Yi, I. Honma, J. Barber and V. Artero, *Nature Materials* 2016 15:6, 2016, **15**, 640–646.
- 17 D. Escalera-López, C. Iffelsberger, M. Zlatar, K. Novčić, N. Maselj, C. Van Pham, P. Jovanovič, N. Hodnik, S. Thiele, M. Pumera and S. Cherevko, *Nature Communications* 2024 15:1, 2024, **15**, 1–13.
- 18 G. Li, D. Zhang, Q. Qiao, Y. Yu, D. Peterson, A. Zafar, R. Kumar, S. Curtarolo, F. Hunte, S. Shannon, Y. Zhu, W. Yang and L. Cao, *J Am Chem Soc*, 2016, **138**, 16632–16638.
- 19 F. Gonell, M. Rodenes, S. Martín, M. Boronat, I. Sorribes and A. Corma, *Chemistry of Materials*, 2023, **35**, 8483–8493.
- 20 G. Schwarz, R. R. Mendel and M. W. Ribbe, *Nature*, 2009, **460**, 839–847.
- 21 Z. Y. Yang, D. R. Dean and L. C. Seefeldt, *Journal of Biological Chemistry*, 2011, **286**, 19417–19421.
- 22 C. Alfonso, R. Llusar and M. Feliz, *Current Inorganic Chemistry (Discontinued)*, 2018, **7**, 106–110.
- 23 T. F. Beltrán, J. Á. Pino-Chamorro, M. J. Fernández-Trujillo, V. S. Safont, M. G. Basallote and R. Llusar, *Inorg Chem*, 2015, **54**, 607–618.
- 24 A. Baloglou, M. Plattner, M. Ončák, M. L. Grutza, P. Kurz and M. K. Beyer, *Angewandte Chemie International Edition*, 2021, **60**, 5074–5077.
- 25 S. Batool, S. P. Nandan, S. N. Myakala, A. Rajagopal, J. S. Schubert, P. Ayala, S. Naghdi, H. Saito, J. Bernardi, C. Streb, A. Cherevan and D. Eder, *ACS Catal*, 2022, **12**, 6641–6650.
- 26 K. Du, L. Zheng, T. Wang, J. Zhuo, Z. Zhu, Y. Shao and M. Li, *ACS Appl Mater Interfaces*, 2017, **9**, 18675–18681.
- 27 F. Gonell, M. Rodenes, S. Martín, M. Boronat, I. Sorribes and A. Corma, *Chemistry of Materials*, 2023, **35**, 8483–8493.
- 28 C. H. Lee, S. Lee, Y. K. Lee, Y. C. Jung, Y. Il Ko, D. C. Lee and H. I. Joh, *ACS Catal*, 2018, **8**, 5221–5227.
- 29 Z. Ji, C. Trickett, X. Pei and O. M. Yaghi, *J Am Chem Soc*, 2018, **140**, 13618–13622.
- 30 A. L. Gushchin, R. Hernandez-Molina, A. V. Anyushin, M. R. Gallyamov, J. Gonzalez-Platas, N. K. Moroz and M. N. Sokolov, *New Journal of Chemistry*, 2016, **40**, 7612–7619.
- 31 F. Xi, F. Bozheyev, X. Han, M. Rusu, J. Rappich, F. F. Abdi, P. Bogdanoff, N. Kaltsoyannis and S. Fiechter, *ACS Appl Mater Interfaces*, 2022, **14**, 52815–52824.
- 32 J. Kibsgaard, T. F. Jaramillo and F. Besenbacher, *Nature Chemistry* 2014 6:3, 2014, **6**, 248–253.
- 33 W. Hu, L. Xie, C. Gu, W. Zheng, Y. Tu, H. Yu, B. Huang and L. Wang, *Coord Chem Rev*, 2024, **506**, 215715.
- 34 Y. Lei, M. Yang, J. Hou, F. Wang, E. Cui, C. Kong and S. Min, *Chemical Communications*, 2018, **54**, 603–606.
- 35 A. Baloglou, M. Ončák, M. L. Grutza, C. Van Der Linde, P. Kurz and M. K. Beyer, *Journal of Physical Chemistry C*, 2019, **123**, 8177–8186.
- 36 D. B. Tran, T. H. To and P. D. Tran, *Coord Chem Rev*, 2022, **457**, 214400.
- 37 G. Liu, P. Liu, D. Meng, T. Zhao, X. Qian, Q. He, X. Guo, J. Qi, L. Peng, N. Xue, Y. Zhu, J. Ma, Q. Wang, X. Liu, L. Chen and W. Ding, *Nature Communications* 2023 14:1, 2023, **14**, 1–11.
- 38 G. Liu and J. Wang, *Advanced Energy and Sustainability Research*, 2022, **3**, 2100179.
- 39 E. V. Sukhanova, N. E. Sagatov, A. S. Oreshonkov, P. N. Gavryushkin and Z. I. Popov, *Nanomaterials*, 2023, **13**, 368.
- 40 Y. Ohki, R. Hara, K. Munakata, M. Tada, T. Takayama, Y. Sakai and R. E. Cramer, *Inorg Chem*, 2019, **58**, 5230–5240.
- 41 P. D. Tran, T. V. Tran, M. Orio, S. Torelli, Q. D. Truong, K. Nayuki, Y. Sasaki, S. Y. Chiam, R. Yi, I. Honma, J. Barber and V. Artero, *Nat Mater*, 2016, **15**, 640–646.
- 42 Y. Deng, L. R. L. Ting, P. H. L. Neo, Y. J. Zhang, A. A. Peterson and B. S. Yeo, *ACS Catal*, 2016, **6**, 7790–7798.
- 43 F. Xi, P. Bogdanoff, K. Harbauer, P. Plate, C. Höhn, J. Rappich, B. Wang, X. Han, R. Van De Krol and S. Fiechter, *ACS Catal*, 2019, **9**, 2368–2380.
- 44 V. P. Fedin, B. A. Kolesov, Y. V. Mironov and V. Y. Fedorov, *Polyhedron*, 1989, **8**, 2419–2423.
- 45 A. Müller, V. Wittneben, E. Krickemeyer, H. Bögge and M. Lemke, *ZAAC - Journal of Inorganic and General Chemistry*, 1991, **605**, 175–188.
- 46 T. Weber, J. C. Muijsers and J. W. Niemantsverdriet, *Journal of Physical Chemistry*, 1995, **99**, 9194–9200.
- 47 C. H. Chang and S. S. Chan, *J Catal*, 1981, **72**, 139–148.
- 48 Y. Deng, L. R. L. Ting, P. H. L. Neo, Y. J. Zhang, A. A. Peterson and B. S. Yeo, *ACS Catal*, 2016, **6**, 7790–7798.
- 49 P. Adams, J. Bühler, I. Walz, T. Moehl, H. Roithmeyer, O. Blacque, N. Comini, J. T. Diulus, R. Alberto, S. Siol, M. Dimitrievska, Z. Novotny and S. D. Tilley, *ACS Energy Lett*, 2024, **9**, 3828–3834.
- 50 M. Gutiérrez-Blanco, C. A. M. Stein, C. Alfonso, E. Guillamón, V. S. Safont, I. Sorribes, H. Junge, M. Beller and R. Llusar, *ChemCatChem*, 2023, **15**, e202300740.
- 51 H. Akashi, T. Shibahara and H. Kuroya, *Polyhedron*, 1990, **9**, 1671–1676.

- 52 M. Dave, A. Rajagopal, M. Damm-Ruttensperger, B. Schwarz, F. Nägele, L. Daccache, D. Fantauzzi, T. Jacob and C. Streb, *Sustain Energy Fuels*, 2018, **2**, 1020–1026.
- 53 G. Li, D. Zhang, Q. Qiao, Y. Yu, D. Peterson, A. Zafar, R. Kumar, S. Curtarolo, F. Hunte, S. Shannon, Y. Zhu, W. Yang and L. Cao, *J Am Chem Soc*, 2016, **138**, 16632–16638.
- 54 M. I. Aroyo, J. M. Perez-Mato, C. Capillas, E. Kroumova, S. Ivantchev, G. Madariaga, A. Kirov and H. Wondratschek, in *Zeitschrift für Kristallographie*, 2006, vol. 221, pp. 15–27.
- 55 M. I. Aroyo, J. M. Perez-Mato, D. Orobengoa, E. Tasci, G. De La Flor and A. Kirov, *Crystallography online: Bilbao Crystallographic Server*, 2011, vol. 43.
- 56 M. I. Aroyo, A. Kirov, C. Capillas, J. M. Perez-Mato and H. Wondratschek, *Acta Crystallogr A*, 2006, **62**, 115–128.
- 57 M. Dimitrievska, A. P. Litvinchuk, A. Zakutayev and A. Crovetto, *Journal of Physical Chemistry C*, 2023, **127**, 10649–10654.
- 58 C. Blaga, Á. Labordet Álvarez, A. Balgarkashi, M. Banerjee, A. Fontcuberta i Morral and M. Dimitrievska, *Nanoscale Adv*, 2024, **6**, 4591–4603.
- 59 S. Käser, E. D. Boittier, M. Upadhyay and M. Meuwly, *J Chem Theory Comput*, 2021, **17**, 3687–3699.
- 60 Y. Wu, J. Zhang, T. Zhang, K. Sun, L. Wang, H. Xie and Y. Tan, *Ind Eng Chem Res*, 2019, **58**, 9343–9351.
- 61 L. Maschio, B. Civalleri, P. Ugliengo and A. Gavezzotti, *Journal of Physical Chemistry A*, 2011, **115**, 11179–11186.
- 62 I. Lezcano-Gonzalez, E. Campbell, A. E. J. Hoffman, M. Bocus, I. V. Sazanovich, M. Towrie, M. Agote-Aran, E. K. Gibson, A. Greenaway, K. De Wispelaere, V. Van Speybroeck and A. M. Beale, *Nature Materials* 2020 19:10, 2020, **19**, 1081–1087.
- 63 P. Y. Yu and M. Cardona, *Fundamentals of Semiconductors*, Springer Berlin, Heidelberg, 4th Ed., 2010.
- 64 M. Jiménez-Guerra, L. Calvo-Barrio, J. M. Asensi, I. Caño-Prades, S. Yan, E. Barrena, J. Puigdollers, Z. Jehl, Y. Sánchez and E. Saucedo, *ACS Appl Energy Mater*, 2024, **7**, 874–884.
- 65 P. Adams, R. Schnyder, T. Moehl, J. Bühler, A. L. Alvarez, M. Dimitrievska, K. McKenna, W. Yang and S. D. Tilley, *Adv Funct Mater*, 2024, **34**, 2310596.
- 66 M. B. Costa, M. A. de Araújo, J. Puigdollers, P. Ortega, T. Andreu, C. Voz, E. Saucedo and L. H. Mascaro, *Adv Funct Mater*, 2025, 2506401.
- 67 P. Adams, F. Creazzo, T. Moehl, R. Crockett, P. Zeng, Z. Novotny, S. Luber, W. Yang and S. D. Tilley, *J Mater Chem A Mater*, 2023, **11**, 8277–8284.

Decoding Vibrational Signatures of Molybdenum Sulphide Molecular Catalysts for Solar Hydrogen Evolution

Pardis Adams,^a Jan Bühler,^a Angel Labordet Alvarez,^{b,c} S. David Tilley^a and Mirjana Dimitrievska^{*b}

^a Department of Chemistry, University of Zurich, Zurich, Switzerland.

^b Transport at Nanoscale Interfaces Lab, Swiss Federal Laboratories for Materials Science and Technology (EMPA), Dübendorf, Switzerland.

E-mail: mirjana.dimitrievska@empa.ch

^c Department of Physics and Swiss Nanoscience Institute, University of Basel, Basel, Switzerland

Table of Contents

General Information	2
Syntheses	2
Substrate preparation.....	2
Synthesis of Sb ₂ Se ₃ Photocathodes	3
Solution Treatment and Catalyst Deposition	3
Morphology and Crystal Characterisation	3
Raman Measurements.....	3
Density Functional Theory (DFT)	3
Additional Figures	4
References	8

General Information

All chemicals were of reagent grade or higher, obtained from commercial sources and used without further purification. Solvents for reactions were of p.a. grade; H₂O was ultrapure from a *Milli-Q® Direct 8* water purification system.

FT-IR spectra were recorded on a *SpectrumTwo* FT-IR Spectrometer (*Perkin–Elmer*); samples were applied as KBr pellets. **High-resolution electrospray mass spectra (HR-ESI-MS)** were recorded on a *timsTOF Pro TIMS-QTOF-MS* instrument (*Bruker Daltonics GmbH*, Bremen, Germany). The samples were dissolved in MeOH at a ca. 50 µg mL⁻¹ concentration and analysed via continuous flow injection (2 µL min⁻¹). The mass spectrometer was operated in the positive or negative electrospray ionization mode at 4'000 V (-4'000 V) capillary voltage and -500 V (500 V) endplate offset with an N₂ nebulizer pressure of 0.4 bar and a dry gas flow of 4 L min⁻¹ at 180 °C. Mass spectra were acquired in a mass range from m/z 50 to 2'000 at ca. 20'000 resolution (m/z 622) and at 1.0 Hz rate. The mass analyser was calibrated between m/z 118 and 2'721 using an *Agilent ESI-L* low-concentration tuning mix solution (*Agilent*, USA) at a resolution of 20,000, giving a mass accuracy below 2 ppm. All solvents used were purchased in the best LC-MS quality. **UV-Vis** spectra were recorded on a *Shimadzu UV-3600 Plus* spectrophotometer.

Syntheses

[Mo₃S₄(H₂O)₉]Cl₄ (1), prepared according to a published procedure^{1,2)}

Caution: Toxic H₂S is evolved during the reaction. It is recommended to connect gas-washing bottles containing bleach to the set-up.

A solution of (NH₄)₂[MoS₄] (1.00 g, 3.84 mmol) in H₂O (35 mL) was treated alternately with 1 mL portions of aqueous HCl (6 M, 15 mL) and aqueous NaBH₄ (2 M, 15 mL) under ambient conditions. The resulting brown mixture was heated to 90 °C for 22 h with an oil bath, while compressed air was continuously introduced via a glass syringe. Upon completion, the reaction mixture had turned dark green and was cooled with an ice bath before the resulting precipitate was filtered off and washed with 1 M HCl (10 mL). The combined filtrate was concentrated under reduced pressure to approximately 5 mL and purified by size-exclusion chromatography over a *Sephadex G-10* column (10 g, bloomed in 1 M HCl, eluted with 1 M HCl). A fraction containing the green [Mo₃S₃O]⁴⁺ (λ_{max} 605 nm) eluted first, followed by a darker green fraction (λ_{max} 620 nm) corresponding to the product [Mo₃S₄(H₂O)₉]⁴⁺. The fractions of [Mo₃S₄(H₂O)₉]⁴⁺ were diluted with H₂O (five times the original volume) and purified further by cation-exchange chromatography over a *DOWEX 50WX2* column (15 g, preconditioned with 2 M HCl, eluted with 2 M HCl). A light brown band containing [Mo₂O₂S₂]²⁺ eluted first, followed by the dark green band of the product. Evaporation of the eluent under reduced pressure yielded [Mo₃S₄(H₂O)₉]Cl₄ as a dark green powder (362 mg, 1.28 mmol, 39%).

UV-Vis: λ_{max} (1 M HCl)/nm 255 (ε/dm³ mol⁻¹ cm⁻¹; 7'945), 371 (3'475), 620 (172).

FT-IR (KBr): ν_{max}/cm⁻¹ 3390br, 3225s, 1622m, 1404m, 1195w, 960w, 847m, 806m, 648w, 570w, 549w.

HRMS (ESI): m/z calc. for C₂H₆ClMo₃O₂S₄ [M-9 H₂O+2 OMe+Cl]⁺: 518.60958; found: 518.60871.

(NH₄)₂[Mo₃S₁₃]·2 H₂O (2), prepared according to a published procedure³⁾

A solution of (NH₄)₂S_x (25 wt-%) was prepared by dissolving elemental sulfur (3.00 g) in a solution of (NH₄)₂S (48 wt-%, 20 mL) in H₂O (20 mL). Separately, (NH₄)₂[Mo₇O₂₄]·4 H₂O (1.02 g, 825 µmol) was dissolved in H₂O (5 mL), and the freshly prepared (NH₄)₂S_x solution (25 wt-%, 30 mL) was added. The reaction flask was covered with a watch glass and heated to 95 °C for 96 h with an oil bath and without stirring. Dark red crystals and pockets of elemental sulfur were formed and the solids were isolated by filtration. The filter cake was sequentially washed with H₂O (3×10 mL), EtOH (3×10 mL), CS₂ (3×10 mL, until residual sulfur was fully removed), and Et₂O (3×10 mL). The solid was air-dried to yield (NH₄)₂[Mo₃S₁₃]·2 H₂O as dark red crystals (1.32 g, 1.70 mmol, 88% yield).

UV-Vis: λ_{max} (MeOH)/nm 267 (ε/dm³ mol⁻¹ cm⁻¹; 38'978), 425 (4'432).

FT-IR (KBr): ν_{max}/cm⁻¹ 3437br, 3081m, 2926m, 2781m, 1633w, 1566w, 1399s, 1385s, 544s, 506s, 459w.

HRMS (ESI): m/z calc. for H₃Mo₃S₁₃ [M+3 H]⁺: 712.37607; found: 712.37391.

Substrate preparation

Pilkington's FTO TEC 15 substrates were cut into 1×2.5 cm pieces and cleaned by sonication in H₂O containing alkaline detergent (*Deconex 11 Universal*), H₂O, acetone, and isopropyl alcohol. Subsequently, the substrates were dried with a stream of N₂ and underwent UV/ozone cleaning (30 min) to eliminate surface contaminants.

Synthesis of Sb₂Se₃ Photocathodes

Prepared according to a published procedure.⁴

A *Safematic CCU-010* sputter coater was used to sequentially deposit a 10 nm layer of titanium (Ti) (acting as an adhesion layer) and a 150 nm layer of gold (Au) (serving as a hole-extracting electrode by creating an ohmic contact with the photoabsorber) onto the FTO substrates. The electrodeposition of antimony (Sb) metal was carried out with a three-electrode setup (FTO/Ti/Au stack, Pt wire, Ag/AgCl reference electrode). A solution of potassium antimony tartrate (15 mM) and tartaric acid (50 mM), adjusted to pH 1.3 by addition of H₂SO₄, served as the electrodeposition solution. A potential of -0.3 V versus Ag/AgCl was applied until a charge 1.4 C cm⁻² was passed. Subsequently, the Sb substrates underwent selenisation using a two-zone furnace. Selenium pellets were placed around the substrate, and the chamber was purged with argon. The temperature was increased by 15 °C min⁻¹ up to 350 °C before heating was continued for 40 min at 350 °C.

Solution Treatment and Catalyst Deposition

Before catalyst deposition, the substrate (bare FTO or Sb₂Se₃ photocathode) was immersed into a solution of (NH₄)₂S (10–12 wt%) for 5 s before rinsing with H₂O and drying with a stream of N₂.

Catalyst deposition solutions (1 mM) of [Mo₃S₄(H₂O)₉]Cl₄ ([Mo₃S₄]⁴⁺, 7.20 mg, 0.01 mmol) in aqueous HCl (1 M, 10 mL) and (NH₄)₂[Mo₃S₁₃]·2 H₂O ([Mo₃S₁₃]²⁻, 7.77 mg, 0.01 mmol) in H₂O (10 mL) were prepared by sonication for 30 min. Pre-treated samples were then placed in the catalyst solution for 12 h at ambient temperature. They were then rinsed with H₂O from the backside and annealed at 120 °C for 30 min.

Morphology and Crystal Characterisation

Top-view **scanning electron microscopy (SEM)** and **energy-dispersive X-ray spectroscopy (EDX)** images were acquired using a *Zeiss Gemini 450* SEM device. **X-ray diffraction (XRD)** analysis utilized the *Rigaku Smartlab* diffractometer. Reference cards for Sb₂Se₃ (04-004-7471) and Au (04-004-9181) were obtained from the *Cambridge Crystallographic Data Centre (CCDC)* database.

Raman Measurements

Raman measurements were performed using a *WITec Alpha 300 R* confocal Raman microscope operated in backscattering geometry. All samples were analysed using two excitation wavelengths: 488 and 532 nm. The laser beam was focused onto the sample using a high-numerical-aperture objective, yielding spot sizes of approximately 800 nm for 488 nm and 1 μm for 532 nm excitation. Laser power was carefully optimized to avoid thermal or photo-induced damage: power-dependent studies were conducted by gradually increasing the laser intensity while monitoring for any changes in spectral features such as peak position, broadening, or the appearance of new bands. The highest laser power that did not alter these characteristics was selected for final measurements. Backscattered Raman signals were collected using a 300 mm spectrometer equipped with an 1800 grooves/mm diffraction grating and a thermoelectrically cooled CCD detector. All spectra were calibrated against the Raman signal of a reference silicon sample to ensure spectral accuracy.

Density Functional Theory (DFT)

All density functional theory (DFT) simulations were carried out using *ORCA 6.0.1*.⁵ For each molecular species [Mo₃S₄]⁴⁺ and [Mo₃S₁₃]²⁻, gas-phase geometry optimizations were performed with the *Perdew–Burke–Ernzerhof* (PBE) exchange-correlation functional⁶ in conjunction with the *def2-SVP* basis set.⁷ The resolution of identity (RI) approximation was employed using the matching *def2/J* auxiliary basis set to improve computational efficiency, and the *TIGHTSCF* keyword was specified to ensure tighter self-consistent field (SCF) convergence. All geometry optimizations were done under default optimization criteria, with a maximum of 5000 optimization steps allowed where needed. Following optimization, vibrational frequency calculations were carried out within the harmonic approximation to confirm that each optimized structure was a true minimum (no imaginary frequencies) and to obtain infrared (IR) intensities. Raman activities were computed by enabling numerical frequency calculations (*via NumFreq*) and polarizability derivatives (*via %ELPROP POLAR 1*). Parallelization was performed using between 8 and 32 processes (specified by *%pal nprocs*) to reduce wall-clock time. The resulting IR and Raman spectra were derived directly from the computed vibrational frequencies, dipole derivatives, and polarizability derivatives, providing insights into the vibrational modes of these Mo–S clusters.

Additional Figures

Table S1 Atomic percentages of $[\text{Mo}_3\text{S}_4]^{4+}$ and $[\text{Mo}_3\text{S}_{13}]^{2-}$ on FTO, determined by energy-dispersive X-ray spectroscopy (EDX).

Element	$[\text{Mo}_3\text{S}_4]^{4+}$	$[\text{Mo}_3\text{S}_{13}]^{2-}$
	Atomic %	Atomic %
O	48.8	52.1
Sn	25.0	31.7
C	17.0	10.3
S	3.6	3.4
Mo	3.2	1.1

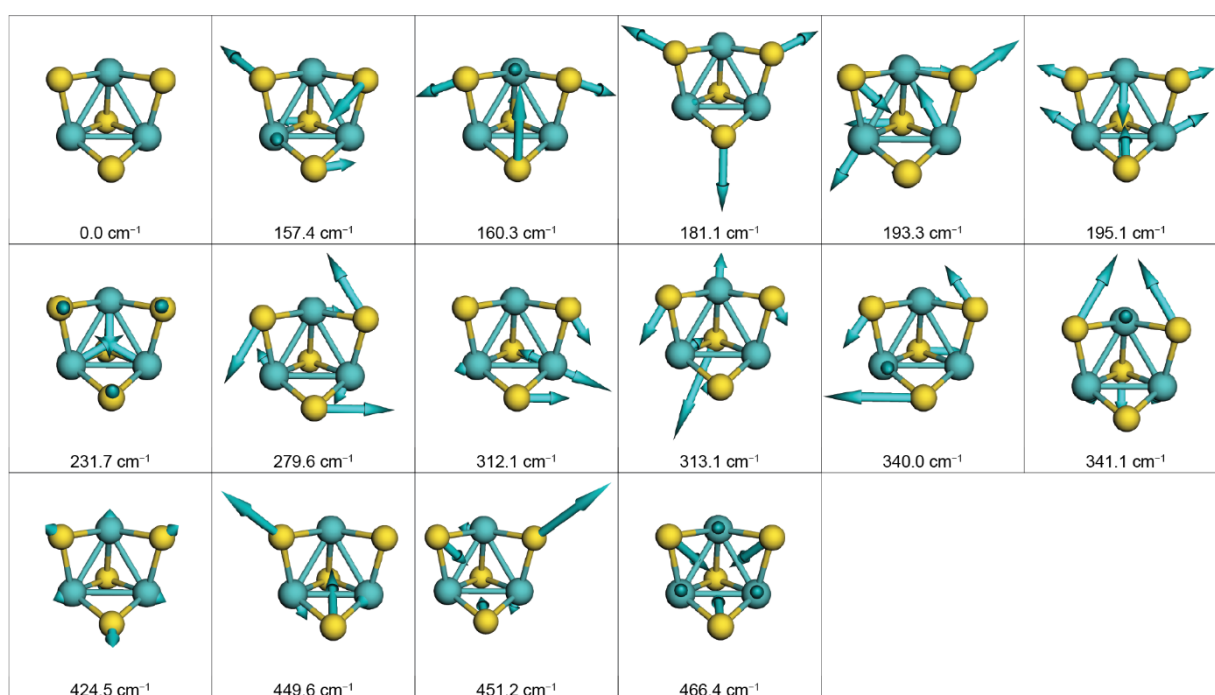


Fig. S1 Calculated phonon displacements for Raman modes of $[\text{Mo}_3\text{S}_4]^{4+}$. Frequencies (in cm^{-1}) are listed under each image.

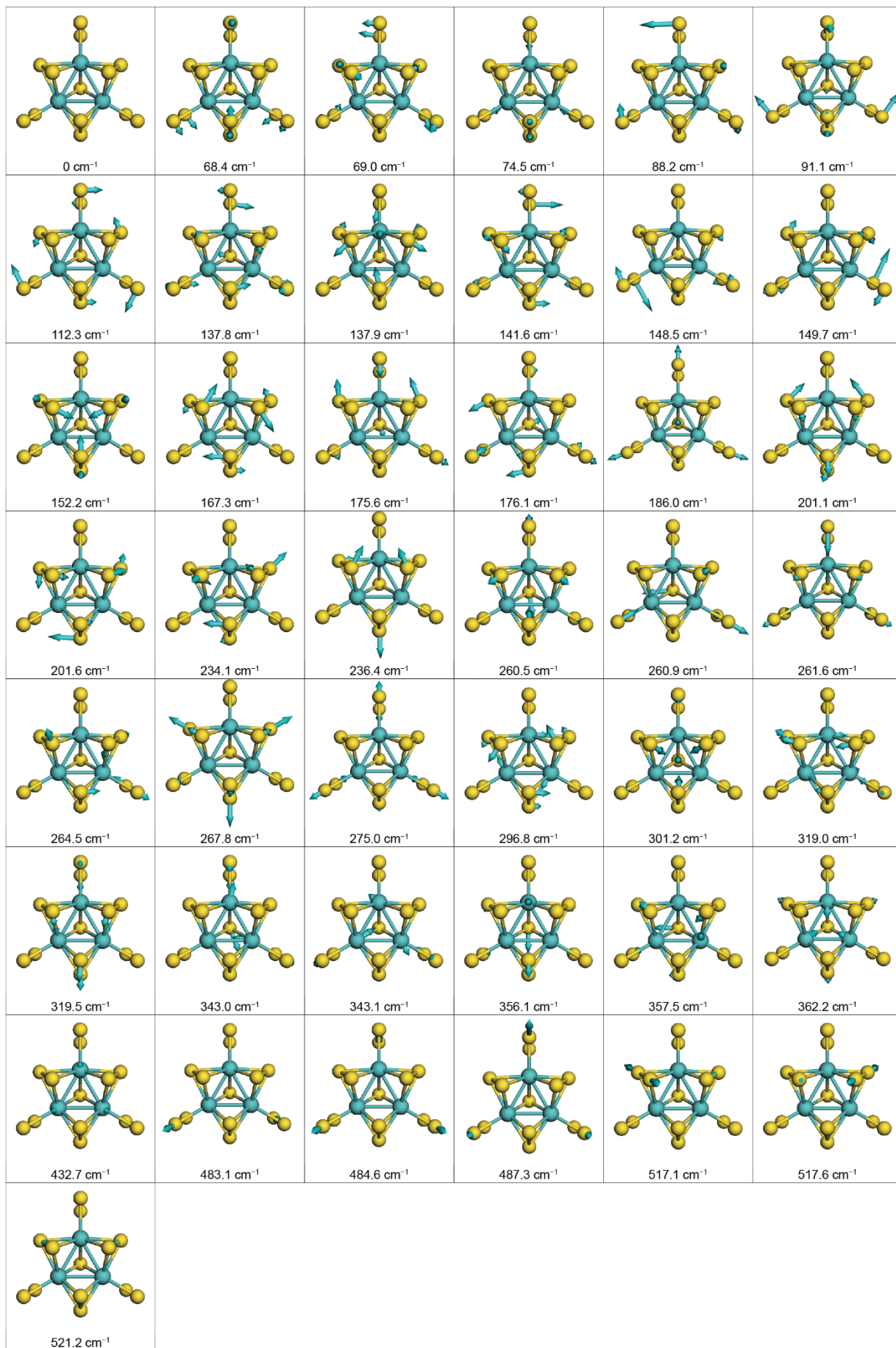


Fig. S2 Calculated phonon displacements for Raman modes of $[\text{Mo}_3\text{S}_{13}]^{2-}$. Frequencies (in cm^{-1}) are listed under each image.

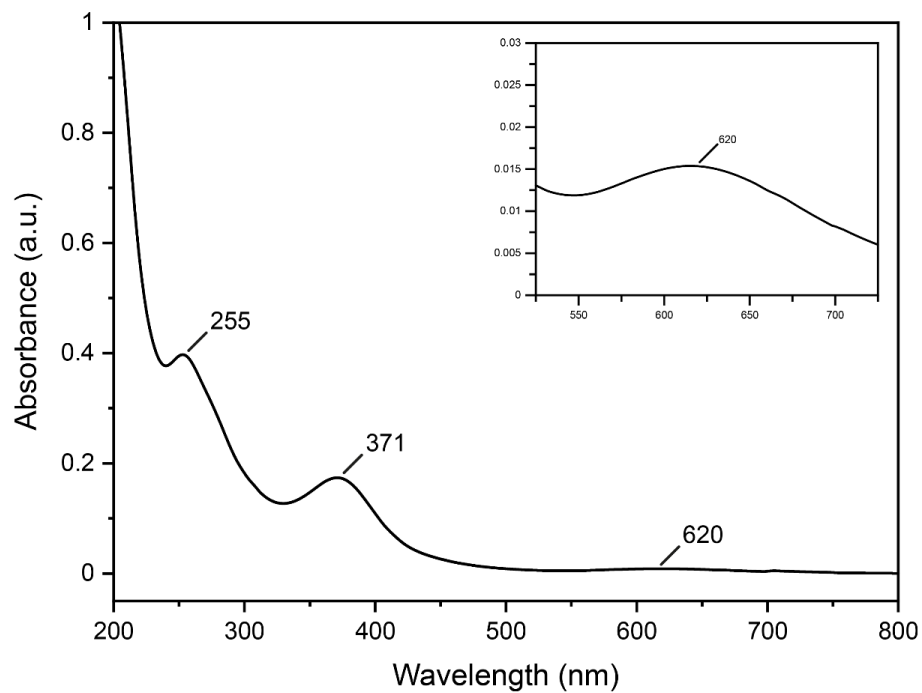


Fig. S3 UV-Vis spectrum of $[\text{Mo}_3\text{S}_4(\text{H}_2\text{O})_9]\text{Cl}_4$ (1), measured in 1 M HCl (50 mM).

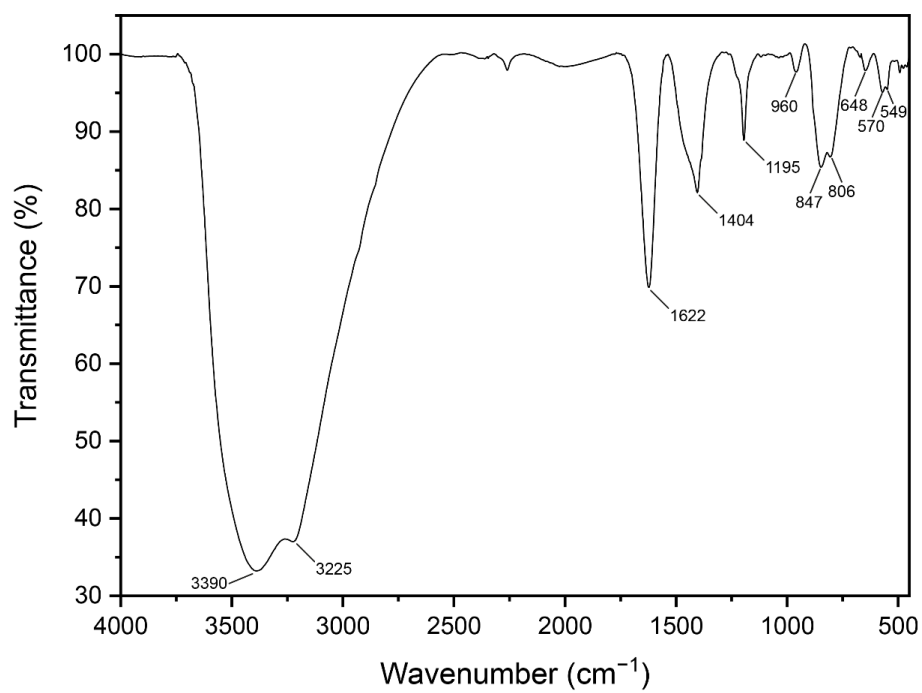


Fig. S4 IR spectrum of $[\text{Mo}_3\text{S}_4(\text{H}_2\text{O})_9]\text{Cl}_4$ (1), measured as KBr pellet.

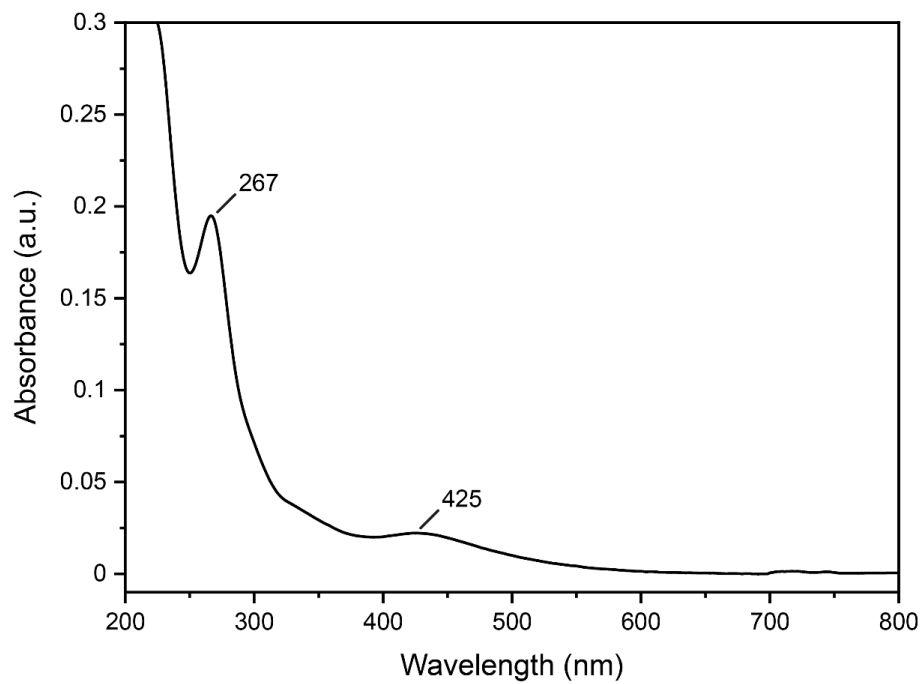


Fig. S5 UV-Vis spectrum of $(\text{NH}_4)_2[\text{Mo}_3\text{S}_{13}] \cdot 2 \text{H}_2\text{O}$ (**2**), measured in MeOH (5 mM).

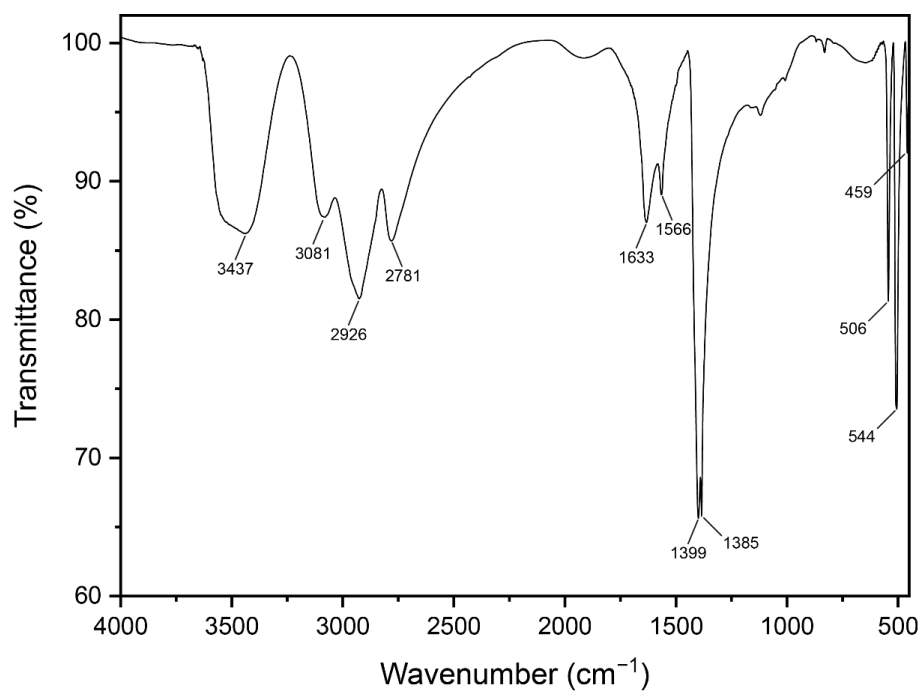


Fig. S6 IR spectrum of $(\text{NH}_4)_2[\text{Mo}_3\text{S}_{13}] \cdot 2 \text{H}_2\text{O}$ (**2**), measured as KBr pellet.

References

- 1 G. Sakane and T. Shibahara, in *Inorganic Syntheses*, ed. D. Coucouvanis, Wiley, 2002, vol. 33, pp. 144–147.
- 2 T. Shibahara, M. Yamasaki, G. Sakane, K. Minami, T. Yabuki and A. Ichimura, *Inorg. Chem.*, 1992, **31**, 640–647.
- 3 M. Dave, A. Rajagopal, M. Damm-Ruttensperger, B. Schwarz, F. Nägele, L. Daccache, D. Fantauzzi, T. Jacob and C. Streb, *Sustainable Energy Fuels*, 2018, **2**, 1020–1026.
- 4 P. Adams, J. Bühler, I. Walz, T. Moehl, H. Roithmeyer, O. Blacque, N. Comini, J. T. Diulus, R. Alberto, S. Siol, M. Dimitrievska, Z. Novotny and S. D. Tilley, *ACS Energy Lett.*, 2024, **9**, 3828–3834.
- 5 F. Neese, *Wiley Interdiscip. Rev.: Comput. Mol. Sci.*, 2012, **2**, 73–78.
- 6 J. P. Perdew, K. Burke and M. Ernzerhof, *Phys. Rev. Lett.*, 1996, **77**, 3865.
- 7 F. Weigend and R. Ahlrichs, *Phys. Chem. Chem. Phys.*, 2005, **7**, 3297–3305.